Egyptian Journal of Geology
https://egjg.journals.ekb.eg

Geochemical Exploration of Copper Mineralization at South Gabal Um Monqul area, North Eastern Desert, Egypt

Attia Rabie [1], Gaber, M. A. Wahab[3], Taher M. Shahin[1] Ashraf Emam[2] and **Mahmoud M. Hassaan[1]**
[1] *Department of Geology, College of Science, University of A-Azhar, Cairo City, Egypt*
[2] *Department of Geology, College of Science, University of Aswan, Aswan City, Egypt*
[3] *Exploration Department, Egyptian Petroleum Research Institute, Cairo, Egypt*

THE South of Gabal Um Monqul area, located in the Northern part of the Eastern Desert of Egypt, is known for Cu-Au mineralization. The rock units are metavolcanics, Dokhan volcanics, and monzogranite. Integrated field, remote sensing, microscopical, and geochemical studies are fulfilled to identify structures, lithological units, hydrothermal alteration zones, and genesis of mineralization. The metavolcanics are metabasalt and meta-andesite. The Dokhan volcanics are represented by andesite and dacite which display fine and porphyritic textures. The monzogranite mainly consists of quartz, plagioclase, orthoclase, and biotite. The remotely sensed data identified the main trends of lineaments, which are NE and NW trend. For the lithological, hydrothermal alteration mapping, the optimum index factor, false color composite, and band ratios techniques effectively distinguish the rock units and identified the alteration types such as argillic, phyllic, and propylitic types. Geochemically, the monzogranites, intermediate metavolcanics and Dokhan volcanics samples showing calc-alkaline while basic metavolcanics showing tholeiitic field. The geochemical patterns and factors distinguished between two fields of ore elements pointing to the presence of these metals more than one phase e.g. sulphides, oxides and silicates. Cu is the chief ore element in metavolcanics; Pb and Mo are the main associated elements, while Ba is the associated element. In the monzogranite, the Cu also is the chief ore element. The primary ore minerals are chalcopyrite, pyrite, magnetite, hematite, titanomagnetite, and ilmenite. Other recorded minerals are barite, chromite, monazite, thorite, molybdenite, and Cd-Se minerals. On the other hand, malachite, chrysocolla, atacamite, and goethite are secondary associations.

Keywords: Copper mineralization, Remote sensing, Um Monqul, Geochemical Exploration.

1. Introduction

The Eastern Desert (ED) of Egypt is part of the Arabian Nubian Shield (ANS), which is divided into three regions: the southern (SD), central (CD), and northern (ND) domains (Stern & Hedge, 1985). The ANS has undergone four major tectonic stages over the past 950 million years (Gass & Ed, 1982; Bentor, 1985; Stern & Kröner, 1993). The first two stages (950–850 Ma and 850–650 Ma) involved rifting, seafloor spreading, and the formation of oceanic crust and island arcs. By the end of the second stage, these oceanic and island arc terranes began to merge. The third stage (650–580 Ma) is characterized by the creation of large-scale calc-alkaline batholiths, which are intermediate to felsic in composition. The fourth stage (600–530 Ma) was characterized by the formation of intracratonic alkaline to peralkaline granites, rhyolites, and multiple dike swarms.

The South of Um Monqul (SUM) area is located at the NED between latitudes 27º 47'and 27º 50'N and longitudes 33º 01' and 33º 09'E (Fig.1). The exposed rock units are mainly granites with few outcrops of metavolcanics and Dokhan volcanics. The area is a type locality for Au mineralization at the NED. Other types of mineralization in the area are recorded in several works such as iron mineralization (Osman, 1994), barite mineralization (Wetait & Botros, 1997) and Cu-Au mineralization (Botros & Wetait, 1997; Abd El-Rahman et al., 2018). Copper and iron mineralization occur in the host rocks, granites, and volcanics, and around quartz veins.

*Corresponding author e-mail: attia.rabie@azhar.edu.eg
Received: 28/01/2025; Accepted: 01/03/2025
DOI: 10.21608/EGJG.2025.356087.1102

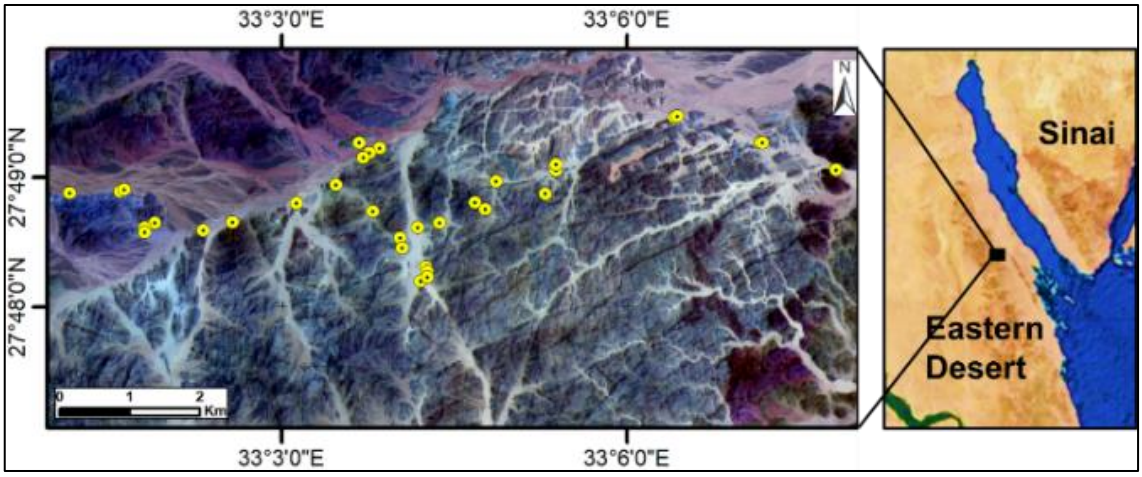

Fig. 1. Location map of the study area (Sentinel 2 image with sample sites).

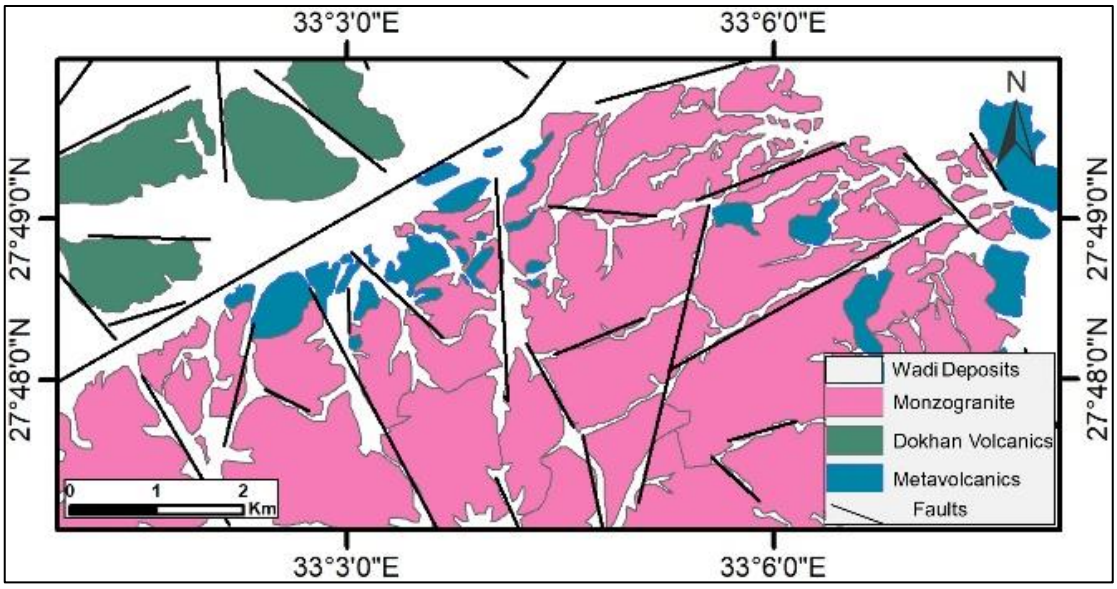

Fig. 2. Geological map of the study area modified after (Botros & Wetait, 1997; Breitkreuz et al., 2010; Abd El-Rahman et al., 2017).

Copper mineralization is found in various metallogenic ore systems. These include magmatic sulfides with copper, nickel, cobalt, and iron (Cu-Ni-Co-Fe), porphyry copper deposits (PCD) with molybdenum and gold (Cu-Mo-Au), low-sulfur iron oxide-copper-gold (IOCG) deposits, and secondary copper deposits enriched by supergene processes and oxide minerals (Pohl, 2011). PCD originated from high-temperature magmatic hydrothermal fluids (Pirajno, 2009). These deposits are distinguished by the presence of sulfide and oxide ore minerals, which form in veinlets and disseminations within extensive volumes of hydrothermally altered rocks (Seedorff et al., 2005, El-Desoky & Hafez, 2018). Moreover, IOCG deposits are a globally important source of copper, gold and critical commodities such as by-product strategic elements including Co, U, and rare earth elements (REEs) (Skirrow, 2022; del Real et al., 2023).

In Egypt's Eastern Desert (ED), copper mineralization occurs in both the southern and northern domains. The southern domain (SED) features Cu-Pb-Zn sulfide deposits in meta-rhyodacite volcanics, such as the Atshan, Darhib, and Um Smiuki mines, as well as the Hamash Cu porphyritic granodiorite. In the northern domain (NED), the Um El Balad, Dara, and South of Um Monqul (SUM) areas are hosted Cu associated with gold.

Osman (1994) recognized three stages of mineralization at SUM area. The oldest is hypogene epithermal gold quartz veins with disseminated Cu-Fe sulfides, then specularite –magnetite associated with Mn oxides. The last stage is characterized by supergene alteration of minerals. The porphyry copper deposit was suggested by Botros & Wetait (1997) based on field, petrographic and chemical characteristics. The rock units were affected by hydrothermal solutions that caused different alteration types such as phyllic, sericite, argillic, potassic, and propylitic types. Moreover, two systems of mineralization were suggested by Abd El-Rahman et al. (2018). The first is old Cu-Mo porphyry system related to the Tonian dacite (MVs) while IOCG system is related to the Ediacaran post-collisional monzogranite.

The hydrothermal alteration types are useful to determine the type of ore deposit such as potassic, phyllic, sodic-calcic, sericite, argillic, and propylitic alterations. These alterations contain mineral assemblages with diagnostic spectral absorption features in the visible - near infrared (VNIR) and shortwave infrared (SWIR) (0.4– 2.5 μm) and/or the thermal infrared (TIR) (8.0–14.0 μm) wavelength regions (Abrams et al., 1983; Spatz et al., 1995). The mineral assemblages can be discriminated from one another by using their spectral absorption features, which are detectable by multispectral and hyperspectral satellite data. The Advanced Spaceborne Thermal Emission and Reflection Radiometer (ASTER) and Sentinel 2 are examples of multispectral satellite data. The ASTER is a remote sensor includes high spectral resolution in the SWIR bands for mapping hydrothermal alteration mineral zones (Pieri & Abrams, 2004). In addition to delineation of hydrothermal alteration zones, the ASTER data are the most useful for lithological mapping and mineral exploration targets, especially for Fe oxides. On the other side, the Sentinel 2 band ratios are proposed to derive the following products: ferric iron, ferrous iron, laterite, gossan, ferrous silicate and ferric oxides hydrothermal alterations, Cu - Au mineralization and lithological mapping (van der Werff & van der Meer, 2016; Forson et al., 2021).

The main objective of the present study is the use of integrated remote sensing, fieldwork, petrographic, and geochemical data for lithological mapping and delineation of hydrothermal alteration zones in the SUM area. Processing techniques will be applied for remotely sensed data of ASTER and Sentinel-2 MSI sensors. The results will be combined with field verification and petrographic description. In addition, the ore microscopical studies will be used to identify the ore minerals forming mineralization and the genesis of mineralization, which previously mentioned as epithermal or PCD or IOCG. The geochemical characteristics of the studied rock units will be investigated especially the trace elements characteristics, to locate and understand the Cu mineralization in the study area.

2. Geological Setting

The exposed rocks in the study area are represented by arc metavolcanics (MVs), Dokhan volcanics (DVs), and granites (Fig. ٢). These rock units are also crossed by abundant mafic and felsic dykes. The arc metavolcanics appear as low to moderate relief and low-lying outcrops that have been intruded by younger granites (Fig.3a). They comprise metabasalt and meta-andesite that are massive to weakly foliated, green to grey in color, and display a porphyritic texture. Secondary copper minerals such as azurite and malachite present as stained forms. These rocks show a moderate level of metamorphism.

Dokhan volcanics (DVs) are exposed at Gabal El Nasb and Gabal Monqul. The age of DVs is 630 ± 6 to 605 ± 6 Ma (Breitkreuz et al., 2010). They form deformed rocks, massive – high relief outcrops relative to the other surrounding rock units. The DVs consist of a series mainly of andesite and dacite, which are fine-grained or porphyritic.

The monzogranite forms an elliptical pluton-like shape and runs approximately NE. There is uncertainty over the SUM granite's chronological order. They could be associated with earlier granite that is syn-tectonic (Osman, 1994; Botros & Wetait, 1997; Eliwa et al., 2014). Meanwhile, Abd El-Rahman et al. (2017) mentioned the age dating of granites is 558+ 4 Ma. The pluton is formed highly weathered granitic rocks with low to moderate topography, highly jointed and exhibits often exfoliation in general (Fig.3b). The outcrop is intersected by numerous dykes, especially in the northeastern region, which exhibit a range of colors and compositions: mafic, intermediate and felsic (Fig.3d). Also, alkali feldspar granites dykes are recorded. Quartz veins are recorded in various sites with copper and iron minerals (Fig.3c).

3. Materials and Methods

The present study used remote sensing data of ASTER (Granule ID: AST L1T 00303182003083631_ 20150427165322_41488, acquired on 18 March 2003) and Sentinel 2B MSI (Granule ID: S2B MSIL1C 20220719T081609_N0400_R121_T36RVR_202207 19T091239 and S2B MSIL1C 20220719T081609_ N0400_R121_T36RWR_20220719T091239, acquired on 19 July 2022). The data have been processed using the ENVI 5.1 (ENVI image processing and analysis software, from ITT Visual Information Solutions) and Sentinel Application

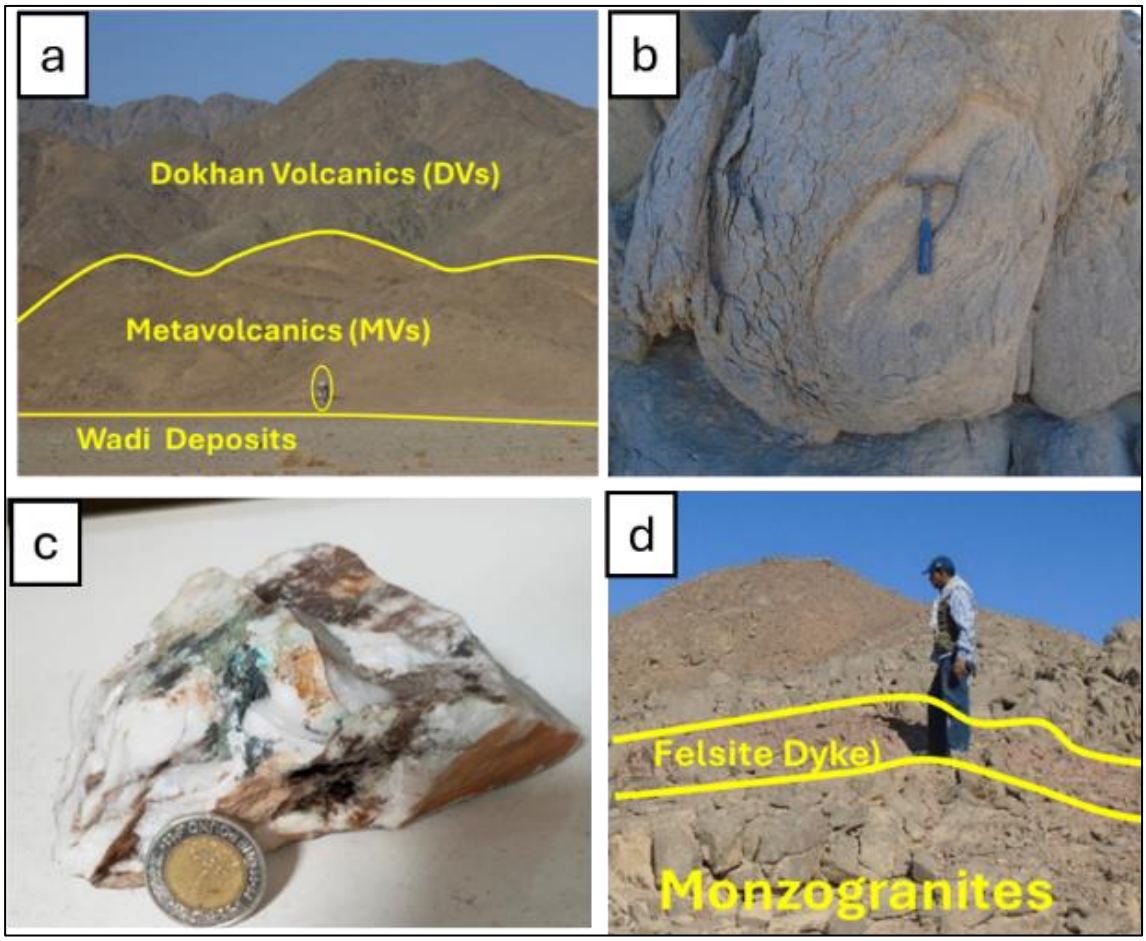

Fig. 3. Field photographs showing a) Low metavolcanic hill compared to DVs. b) Onion-like shape of monzogranit and iron oxides. c) iron oxides and malachite within quartz sample. d) Felsite dyke cutting monzogranite.

Platform (SNAP) software version 8, in addition to the PCI Geomatica 2018 software for the automated lineaments extraction.

Three types of corrections have been done for ASTER data: crosstalk, radiometric and atmospheric FLAASH corrections using the ENVI 5.1 software. The band Ratio (BR) was applied for detecting iron oxides and hydrothermal alteration zones.

Mineralogical Indices using ASTER SWIR bands were applied by (Ninomiya, 2003) for mapping hydrothermal alteration. These indices include: OH-bearing minerals index OHI = (Band7/Band6)*(Band4/Band6), alunite index ALI = (Band7/Band5)*(Band7/Band8), kaolinite index KLI = (Band4/Band5)*(Band8/Band6), and calcite index CLI = (Band6/Band8)*(Band9/Band8). The false color composite (FCC) is an image enhancement technique where the three additive colors of red, green and blue were used to display multispectral bands, where the minerals show a maximum in their spectral reflectance. The possible color composites (R-G-B) of nine ASTER (SWIR and VNIR) are 84. For highlighting the best combinations of color composite based on information, the optimum index factor (OIF) was used to select the optimum combination of three bands a satellite image to produce a color composite (Chavez et al., 1982; Emam et al., 2018). To calculate the OIF highest ranking, the ILIWS software was used.

During the field work, sampling, and structural measurements were carried out, 54 representative samples were collected from the different rock units. Forty samples were prepared for making thin sections and polished surfaces to study the mineral constituents and ore minerals using polarizing, ore microscopes and Environmental Scanning Electron Microscope (ESEM). Moreover, for analysing major and trace elements, seventeen samples were crushed and well pulverized using the normal sequence of the fractionation. The analyses were performed using an XRF Multi-purpose Benchtop Sequential Wavelength Dispersive X-Ray Fluorescence (XRF) spectrometer (Supermini 200 model, manufactured

by Rigaku, Japan). This XRF spectrometer operates under vacuum/helium conditions and is equipped with a 200 W x-ray tube. The analyses were conducted at the Egyptian Petroleum Research Institute (EPRI), Cairo, Egypt.

The correlation coefficient and correlation fields were used to understand the degree of relationships between the trace elements. The Clarke of concentration (CC) is a factor to distinguish the anomalous from the normal geochemical background samples for each rock unit. The CC was calculated dividing the concentration of the elements in the samples of the studied rock units by the reference that given by Turekian & Wedepohl (1961). The element content is normal when CC value between 0.5 and 1.78 (Kviatkovisky, 1977; Hassaan et al., 1991). The element having CC value < 0.5 or >1.78 is to be considered negatively or positively anomalous respectively. The CC values would be also used to distinguish the geochemical association of mineralization.

4. Results

4.1 Remote Sensing

Remote sensing techniques were applied to the ASTER and Sentinel-2B MSI data to show the spectral aspects of the study area which are beneficial in lithological mapping and delineation of mineralization zones.

4.1.1 Lineaments Extraction

The structural lineaments representing major faults in the study area were manually traced from the processed false color composite images of ASTER bands (R: 7, G: 3, B: 1) and Sentinel-2B bands (R: 12, G: 8, B: 3), (Fig.4a). Moreover, the automated extraction of lineaments was carried out using computer software PCI Geomatica version 16 (Fig.4b). The SUM area is a part of the ANS that was affected by the Red Sea graben systems. The main fault systems observed in the NE and NW directions.

The faults comprise the dry valleys (wadis) of the area (Fig.4a). Moreover, the line density map was created to highlight the densest structure areas occurred mainly to the east in monzogranite and metavolcanics. (Fig.4c). The trend analysis using rose diagram (Fig.4d) shows two main directions, the first is NE while the second is NW; these extracted trends are the same as the results of manual lineaments extraction.

4.1.2 Lithological mapping

For the lithological mapping, the ASTER and Sentinel-2B data were processed using the optimum index factor (OIF), false color composite (FCC), and band ratios techniques. The results of OIF algorithm applied for the ASTER and Sentinel-2B reflected VNIR-SWIR bands show six false color band combinations with highest OIF values (Table 1).

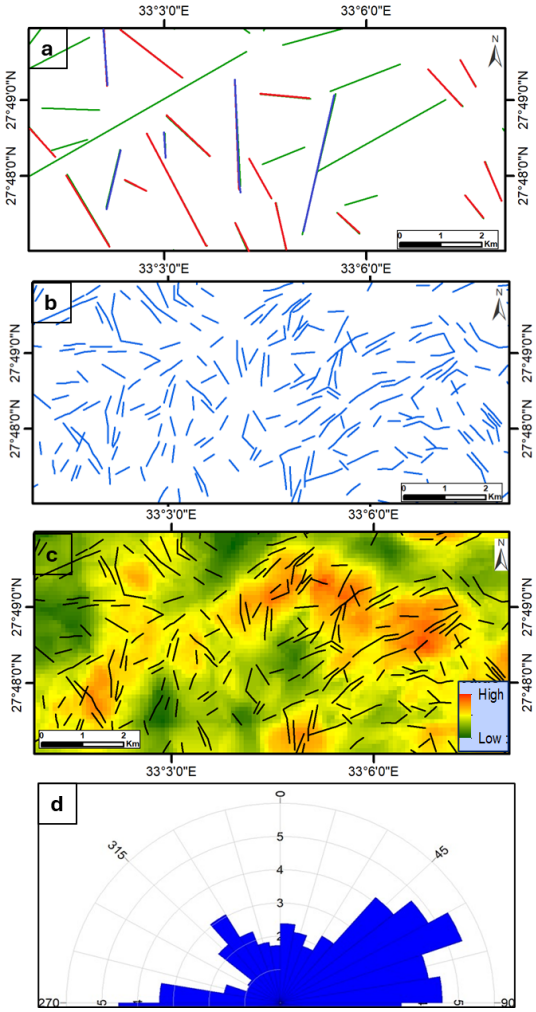

Fig. 4. Photograph showing a) Manual extracted lineaments. b) Automated extracted lineaments. c) Line density map showing the highly structure areas with automated lineaments. d) Rose diagram showing the main trend directions.

According to the OIF results, the ASTER band combinations (R: 8, G: 6, B: 1) and (R: 9, G: 2, B: 1), as well as the Sentinel-2B band combinations (R: 12, G: 11, B: 2) and (R: 12, G: 4, B: 2) discriminate clearly the different rock units occupying the study area. However, the Sentinel 2B band combinations have higher spatial resolution than ASTER band

combinations, so they are recommend being used for distinguishing the rock units (Fig.5a & 5b).

The ASTER FCC image (R: 4/7, G: 3/4, B: 2/1) well discriminates the Dokhan volcanics (DVs) with dark green color, while the ASTER FCC image (R: 4/7, G: 4/1, B: 2/3*4/3) distinguishes the metavolcanics (MVs) as red color (Figs.6a & 6b). The Sentinel 2B FCC image (R: 3, G: 11, B: 12) illustrates all rock units, where metavolcanics as brown color, the Dokhan volcanics as blue color while monzogranite appears as dark green color (Fig.6c).

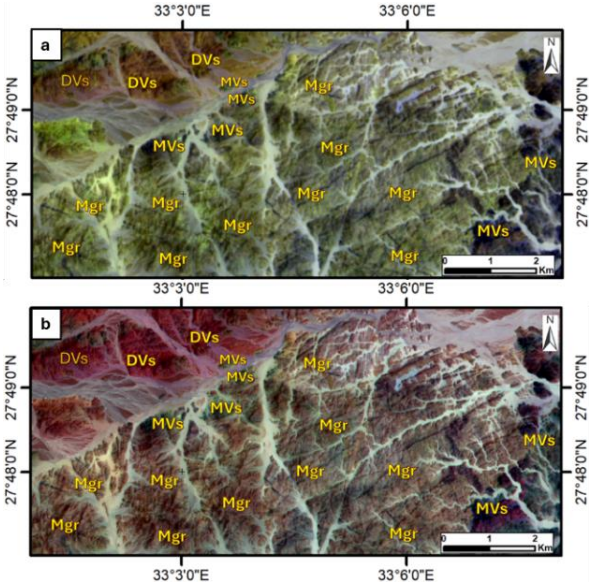

Fig. 5. Photograph showing the OIF results Sentinel 2B data. a) Sentinel 2 OIF 12/11/2. d) Sentinel 2 OIF 12/4/2.

Table 1. OIF index highest ranking of ASTER and Sentinel 2B (VNIR-SWIR) bands.

Data	ASTER				Sentinel -2B			
N	R	G	B	Ratio	R	G	B	Ratio
1	B9	B8	B1	77.00	B12	B4	B2	73.91
2	B9	B2	B1	76.4	B12	B11	B2	73.86
3	B8	B2	B1	76.31	B12	B8	B2	73.82
4	B8	B7	B1	76.26	B12	B3	B2	76.66
5	B8	B6	B1	76.22	B11	B4	B2	73.58
6	B9	B7	B1	76.16	B11	B8	B2	73.49

4.1.3 Mapping hydrothermal alteration zones

Remote sensing data can be utilized to detect and delineate the hydrothermal alteration zones like argillic, phyllic and propylitic types.

The propylitic alteration (450 to 600ºC) can be mapped using the ASTER ratio for epidote and chlorite minerals while calcite index (CI) was used for mapping carbonatized zones (Figs.7a & 7b). The Propylitic alteration zones occur mainly in the Dokhan volcanics at the northwest of the area. Epidote, chlorite, and calcite are the essential minerals with pyrite in many cases. Th iron oxides, sericite and apatite are also present (Ridley, 2013). The phyllic alteration can be mapped using the ASTER band ratio (7/6) and the OH index for discriminating the muscovite and other OH bearing minerals (Figs.7c & 7d). The phyllic alteration zones occur in most parts of the study area, mainly in monzogranite. The phyllic alteration (200 to 450ºC) is characterized by quartz-sericite-pyrite (QSP), where the fine grained dioctahedral white micas (muscovite) are known as sericite (Pirajno, 2009).

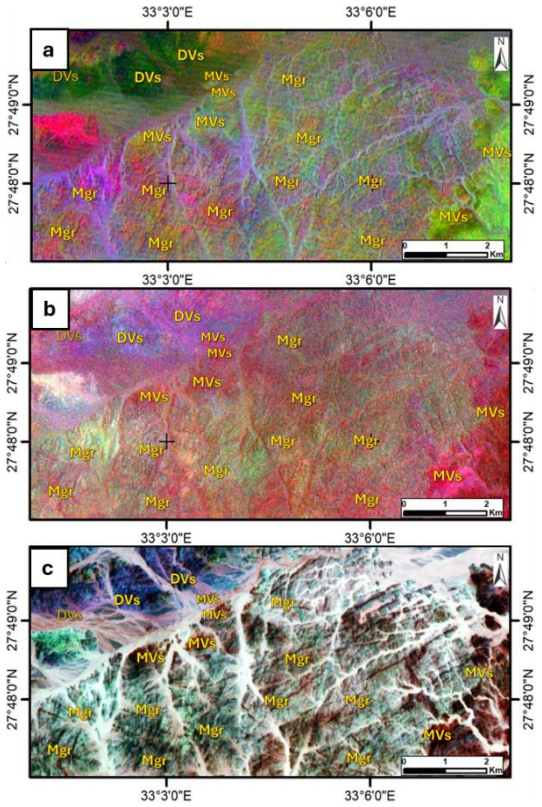

Fig. 6. The FCC images of lithological mapping. a) (4/7, 3/4, 2/1) ratio of Abrams et al., (1983). b) (4/7, 4/1, 2/3*4/3) ratio of Sultan et al., (1986). c) Sentinel 2 bands (3/11/2).

The argillic alteration (100 and 300ºC) can be mapped using the ASTER band ratio (4/6) that clearly discriminates the clay minerals. Moreover, the kaolinite index (KI) is used for mapping kaolinite (Figs.8a & 8b). The processed ratios indicate that the argillic alteration zones are located at the west of the area. In the argillic alteration, kaolinite and montmorillonite are the main clay minerals, with subordinate amounts of other minerals like biotite, illite, chlorite, pyrophyllite, diaspore, alunite, sulfides, quartz and andalusite (Ridley, 2013).

For mapping the hydrothermal alteration zones, Sentinel-2B band ratio (11/12) are used with

combination of mineralogical indices (OH/ KI/CI) (Fig.8c & 8d).

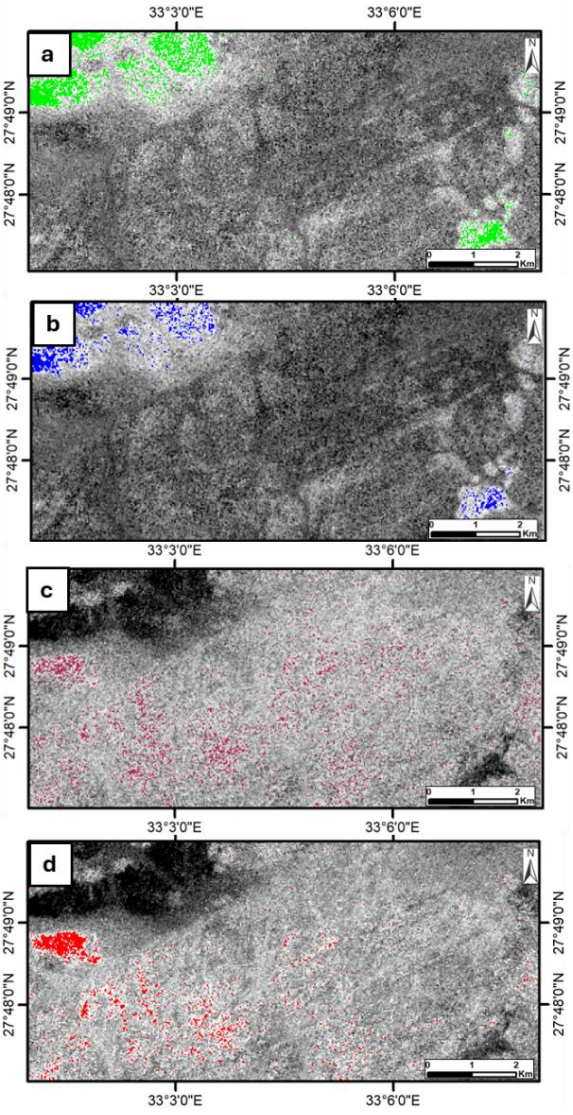

Fig. 7. The ASTER images of Hydrothermal alteration zones. a) 6+9/8 epidote-chlorite. b) Calcite index. c)7/6 muscovite. d) OH index.

The ferruginous alteration is recognized using the Sentinel-2 bands equivalent to ASTER bands for detecting iron bearing minerals. Ferric iron minerals concentrate at most parts of the area, mainly in monzogranite (Fig.9a). Iron oxides and gossans occur in the Dokhan volcanics at the northwest of the area (Figs.9b & 9c). The use of equivalent band ratios of Sentinel 2B and ASTER revealed results with the same occurrences, but the Sentinel 2B images are showing high resolution due to the properties of Sentinel 2B MSI.

4.2 Microscopic Studies

The microscopical studies include the use of polarizing (petrographic) microscope for studying the host rock mineral composition and textures while ore microscope and ESEM are used to identify the ore minerals.

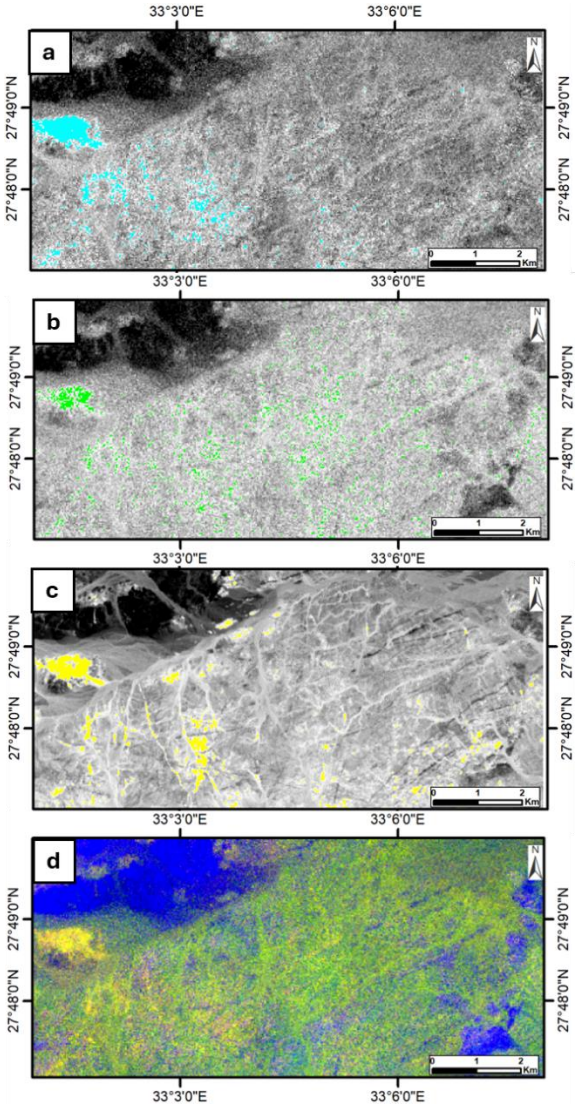

Fig. 8. The ASTER images of Hydrothermal alteration zones. a) 4/6 clay minerals. b) Kaolinite index c)11/12 of Sentinel 2B Alteration zones. d) RGB (OH/Kl/Cl) image of the combined indices.

4.2.1 Petrography

The arc MVs are represented by meta-basalt and meta-andesite. The meta-basalt is composed essentially of plagioclase and pyroxene with minor olivine, calcite, epidote and opaque minerals. Plagioclase occurs as prismatic laths, or porphyroblast crystal in fine grained groundmass (Fig.10a). The plagioclase deformed and altered to epidote. Pyroxene is characterized by two sets of cleavage and high interference colors (Fig.10b). Calcite occurs as filling vesicles as amygdaloidal

texture (Fig.10c). Epidote is generally present as fine to very fine-grained crystals filling microveinlets.

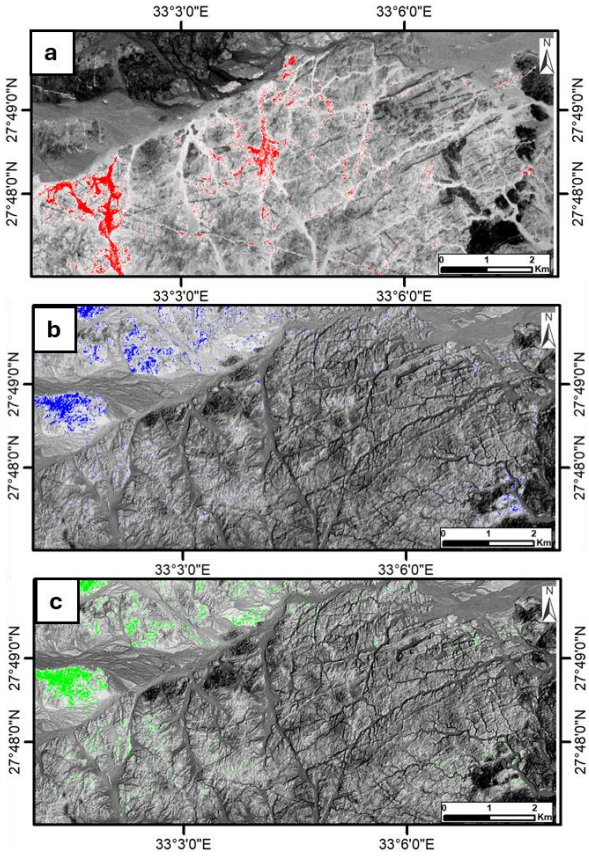

Fig. 9. Photograph showing the iron bearing minerals. a) Ferric iron minerals Sentinel 2B 4/2. b) Iron oxides Sentinel 2B 11/8. c) 4/2 Gossan Sentinel 2B 11/4.

The meta-andesite is a gray green that displays a porphyroblast texture. Its composition primarily consists of plagioclase and hornblende embedded within a groundmass. The quartz and iron oxides are accessory minerals. Secondary minerals include. The quartz and iron oxides are accessory minerals. Secondary minerals include chlorite and epidote. Plagioclase crystals are tabular in shape and can be sub idiomorphic or xenomorphic, reaching up to 1 mm length and up to 0.6 mm width. The less altered crystals exhibit zoned and Carlsbad twinning. Hornblende appears in the form of subidiomorphic prismatic crystals or irregular aggregates. It exhibits pleochroism, ranging from pale green to green (Fig.10d).

The DVs are represented mainly by andesite which consists essentially of plagioclase, hornblende and biotite while the accessory minerals are mainly represented by the iron oxides and characterized by welded texture (Fig.10e). Chlorite and epidote are the main secondary minerals. Plagioclase is ranging in composition from oligoclase to andesine. It is represented by sub idiomorphic altered and deformed crystals up to 1 mm in length and 0.5 mm in width (Fig.10f). Hornblende is present as irregular aggregates.

Monzogranites are medium to coarse grained of hypidiomorphic texture with subordinate perthitic and micro-graphic textures. It consists mainly of plagioclase, quartz, orthoclase, microcline perthite, hornblende and biotite as essential minerals (Fig.10g). Some secondary minerals such as chlorite, and epidotes are recorded as alteration products. The accessory minerals are represented by sphene, zircon and apatite. Plagioclase is mainly oligoclase in composition with an anorthite content varying from (An14) to (An20) that is represented by euhedral and subhedral elongate and tabular crystals. Often plagioclase crystals are deformed, cracked and sometimes altered, so that their lamellar twinning has disappeared. Quartz occurs as medium to coarse grained anhedral, filling often the interstitial spaces of the rock constituents. Sometimes, quartz crystals are cracked and show wavy extinction. Orthoclase occurs as medium grained euhedral crystals, up to 1.5 mm in length and 1 mm in width. Occasionally, it is characterized by simple twinning, partly altered to sericite and kaolin. Microcline–perthite is represented by coarse subhedral crystals.

The perthite comprise vein, flame and patchy types (Fig.10h). Biotite occurs as yellowish brown subhedral flaky crystals. Hornblende is present as irregular aggregates. It shows pleochroism from pale green to green. Sphene is represented by sphenoid shape, high relief (Fig.10i). Zircon and apatite are the common inclusions in the biotite. Iron oxides occur as fine-grained black dots within the rock and between the mineral constituent.

4.2.2 Ore Mineralogy

The magnetite rich titanium is the chief oxide minerals in the arc MVs. It occurred as subhedral to anhedral crystals (Fig.11a & b). Ilmenite is present as euhedral to prismatic lath (Fig.11c). Apatite is a distinctive feature, which occurs as elongated crystals with ilmenite (Fig.11d). Sulfides are recorded with minor amounts. Pyrite occurred as subhedral fractured crystal with anhydrite inclusion (Fig.11e & f). Also, subhedral pyrite is altered to iron oxides (Fig.11g). Chalcopyrite is recorded as minute crystals (Fig.11h).

In monzogranites, magnetite occurred as subhedral crystals, fractured and altered to Ti- magnetite (Figs.12a-c) while ilmenite is occurring as euhedral crystal (Fig.12d). Rutile is present as euhedral to anhedral (Figs.12e & f). The recorded titanium minerals are represented by titanite with chrysocolla (Fig.12g). Secondary Cu minerals are represented by chalcocite and chrysocolla (Fig.12h).

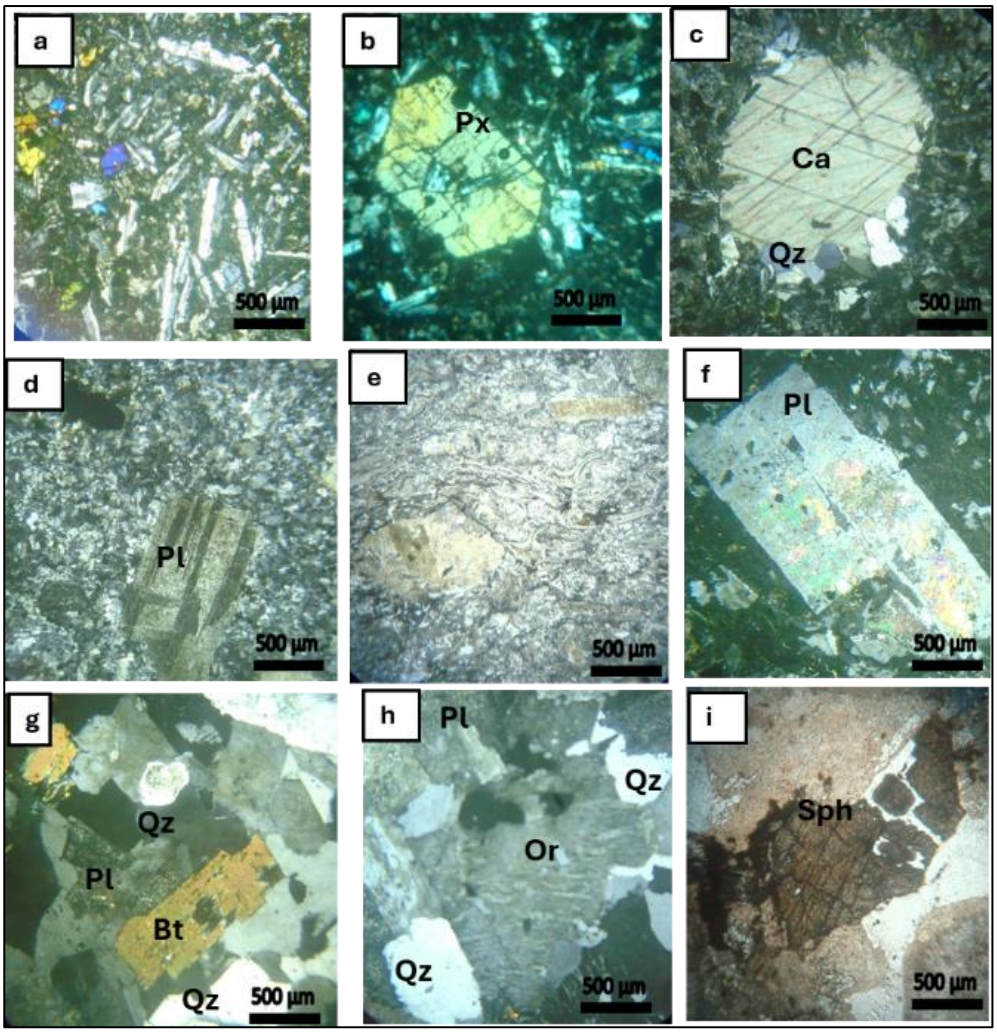

Fig.10. Photomicrograph of the studied rock units showing; a) Plagioclase (Pl) laths with olivine and pyroxene (px). b) Pyroxene (Px) crystals showing high interference colors in groundmass of basic metavolcanics c) amygdaloidal calcite (Ca) crystals with quartz (Qz). d) Plagioclase (Pl) showing lamellar twining in groundmass of meta-andesite. e) Warm-like shape with rock fragments in DVs. f) plagioclase altered to epidote and carbonates in DVs. g) Hypidiomorphic texture in monzogranite with quartz, (Qz), plagioclase (Pl) and biotite (Bt) crystals. h) Orthoclase (Or) showing perthitic texture with quartz (Qz) and plagioclase (Pl). i) Subhedral sphene (Sph) crystal characterized by high relief.

Zircon is surrounded the rutile or associated with euhedral magnetite (Figs. 12e & 13a). Thorite occurred with zircon or as minute crystal (Figs. 13a & b). Barite occurred with molybdenite or within chrysocolla (Figs. 13c &d). Monazite and Cd-Se minerals are recorded (Figs.13e & f).

The sulfides and iron oxides are the main ore minerals within quartz veins. Chalcopyrite occurred as minute crystals within quartz crystals (Figs.14a &b). The secondary copper minerals are represented by chalcocite, malachite, and atacamite. Chalcocite is filling microfractures (Figs.14c & d) while malachite recorded within iron oxides is alteration products (Fig.14e). Specularite (micaceous) hematite is the main iron oxide mineral (Figs.14e). Chromite occurred with small barite inclusion occurred within (Fig.14f).

3.3: Geochemical Investigations

3.3.1: Petrochemical characteristics

The eighteen chemical analyses of the studied rocks at SUM area (Table 2) are used to distinguish the petrochemical features; rock types, magma type and tectonic setting.

The total iron content is high for the basic MVs samples ranging from (11 to 21 wt. %). While the granites show values (3.9- 11.31 wt. %). The area is characterized by the formation of iron oxides and gossan. Iron minerals were recorded in the field and polished surfaces. K_2O shows high values at mineralized granite up to 9.11 and 10.3 %. That may be related to the abundance of K feldspars and mica

minerals in monzogranites in addition to potassic alteration that recorded in mineralized granite.

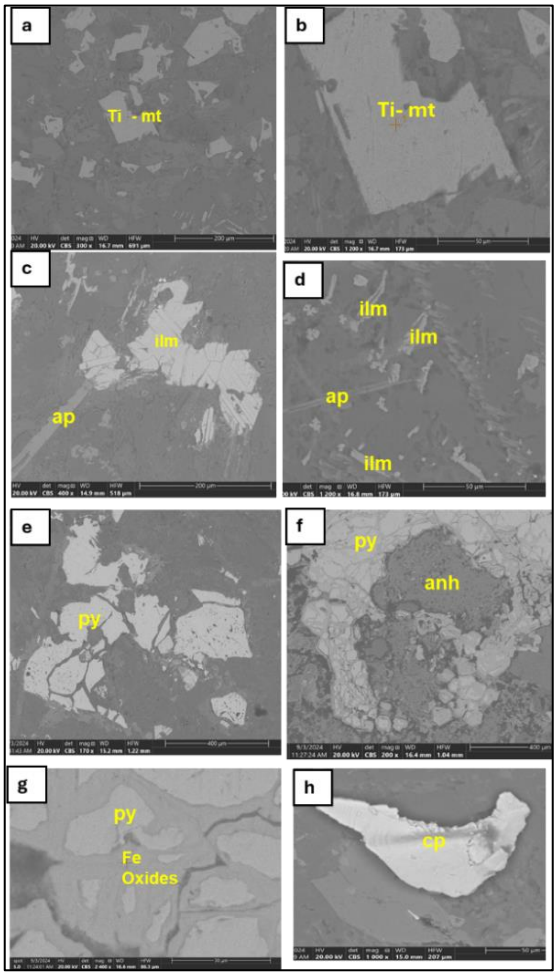

Fig. 11. ESEM Photomicrographs of ore minerals in arc metavolcanics. a & b) Ti-Magnetite minerals in metabasalt. c) Subhedral ilmenite crystal with apatite. d) Ilmenite with elongate apatite crystal. e) Fractured pyrite crystal. f) Anhydrite within pyrite. g) Pyrite altered to iron oxides. h) Small chalcopyrite crystal.

Moreover, the K_2O/Na_2O ratio exhibits values more than 1 (1.5 to 8.76) in granite (Table 2).For the volcanic rocks, the binary relationships of Middlemost (1994) and ternary diagram of Jensen (1976; Figs.15a & 15b) distinguished the rock types as basalt, picro-basalt, high-Fe tholeiitic basalt, dacite and rhyodacite for the MVs. Meanwhile the DVs are classified as dacite and trachy-dacite. On the diagrams of Frost & Frost (2008; Figs.16a & b) the rocks are ferroan for the DVs and intermediate MVs while magnesian nature for most granitic rocks, alkalic for most rocks except intermediate MVs. On the AFM diagram (Irvine & Baragar, 1971) the intermediate MVs, DVs, and granites samples showing calc-alkaline, while basic MVs showing tholeiitic field (Fig.16c).

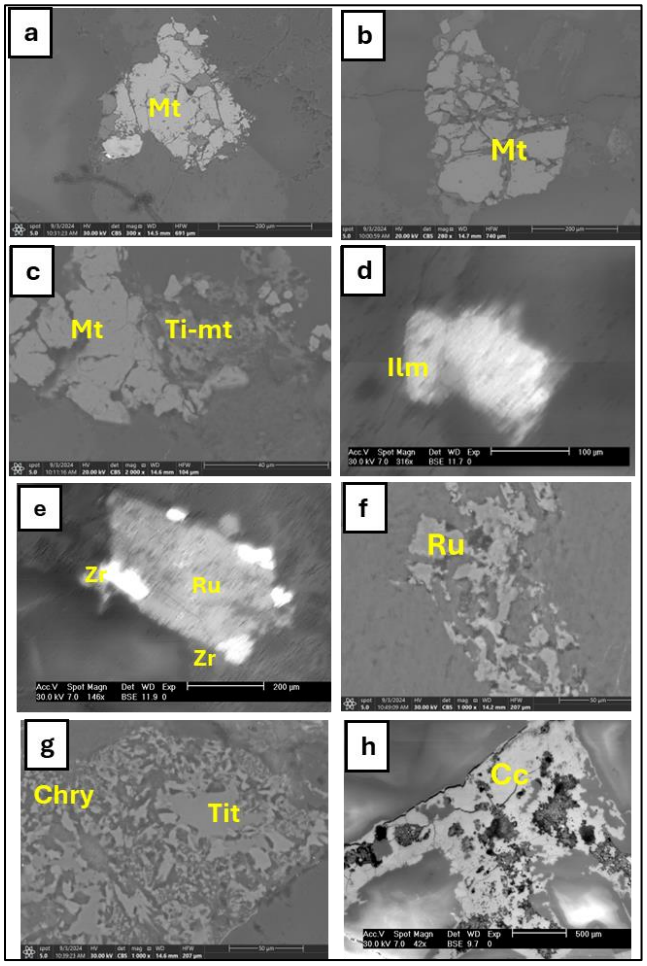

Fig. 12. ESEM Photomicrographs of ore minerals in granites. a & b) Subhedral to euhedral magnetite. c) Magnetite altered to Ti- magnetite. d) Ilmenite crystal e) Rutile altered to zircon at the edges. f) Rutile. g) Titanite with chrysocolla. h) Chalcocite.

Moreover, the (A/NK) versus (A/CNK) binary diagram of Shand (1943) differentiated the study rocks to metaluminous except one monzogranite sample, which is peraluminous (Fig.16d).

For the volcanic rocks, the DVs are formed in spreading center while continental for basic MVs using FeOt, Al_2O_3, and MgO plot of Pearce et al. (1977, Fig.17a). The analyzed samples using the R1-R2 binary diagram (Batchelor & Bowden, 1985) distinguished the tectonic setting of granites as late orogenic granites (Fig.17b).

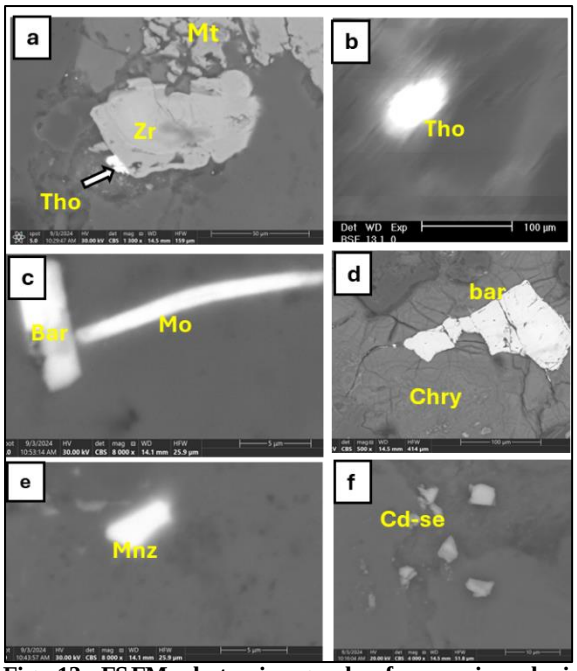

Fig. 13. ESEM photomicrograph of ore minerals in granites. a) Zircon with thorite. b) Minute thorite crystal. c) Molybdenite with barite. d) Barite within chrysocolla. e) Monazite. f) Association of Cd- Se minerals.

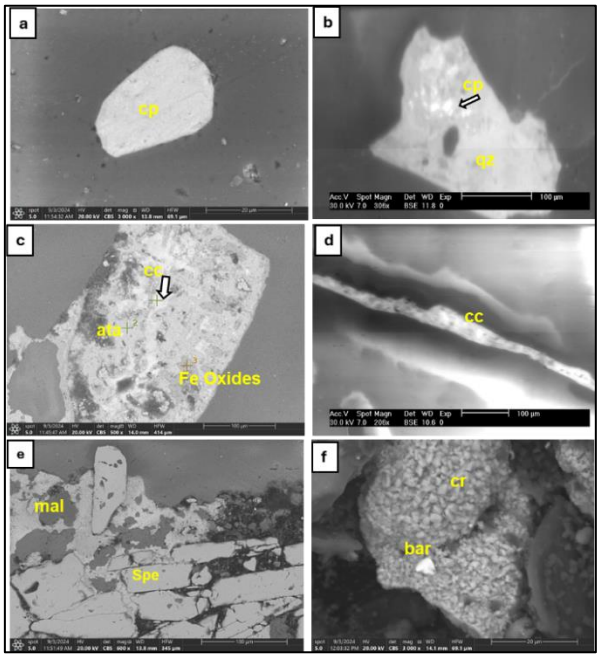

Fig. 14. ESEM Photomicrographs of ore minerals in quartz veins. a) Euhedral chalcopyrite crystal. b) Chalcopyrite within quartz crystal. c) Chalcocite, atacamite and Fe oxides. d) Chalcocite filling fractures. e) Malachite with iron oxides (specularite). f) Chromite with minute barite crystal.

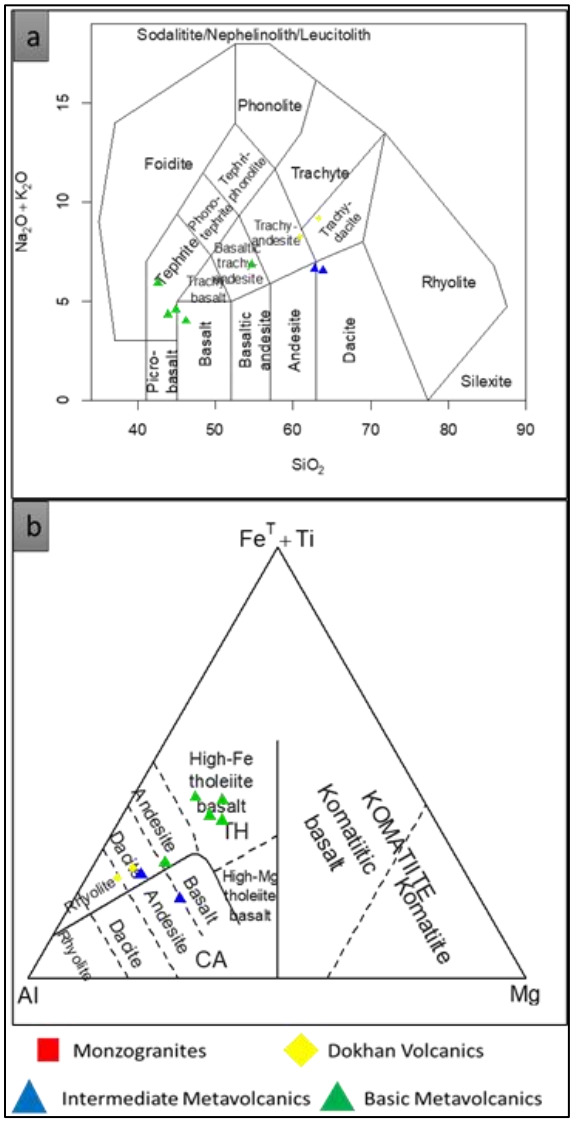

Fig. 15. (a) SiO_2 versus (Na_2O + K_2O) diagram of Middlemost (1994). b) Ternary diagram of (Fe+ Ti) - Mg - Al of Jensen (1976).

4.3.2: Geochemical characteristics of trace elements distribution

Hassaan et al. (1990, 2022 & 2011) used the statistical parameters, Clark of concentration, correlation coefficient, and zoning sequence of deposition to measure and reveal the characteristic behavior of trace elements. These are also used to delineate the zone of mineralization.

Table 2. The chemical analysis of major and trace elements for the studied rock units.

Rock Types	Basic MVs					Intermediate MVs		DVs		Monzogranite								Qz vein
Oxides	45	55.1	71	72	70	64	67	73	74	46.1	49.1	58	51	52	53	54	65	64.1
SiO_2	45.18	42.57	42.51	40.71	52.86	60.99	62.04	61.75	59.34	65.32	61.64	58.37	60.38	60.29	57	55.01	59.66	95.04
TiO_2	0.74	2.08	2.71	2.43	0.93	0.49	0.53	0.57	0.75	0.48	0.65	0.88	1.02	0.67	0.75	0.66	0.58	-
Al_2O_3	13.53	14.2	14.9	14.85	15.72	15.41	15.37	14.96	15.63	14.42	14.58	15.09	13.59	14.51	13.5	14.38	13.81	0.55
Fe_2O_3	21	16.89	17.04	19.03	10.26	6.92	8.35	7.2	8.73	3.91	5.92	6.5	8.09	5.64	8.53	11.31	7.78	2.2
MnO	0.37	0.24	0.27	0.34	0.15	0.1	0.09	0.14	0.17	0.06	0.1	0.08	0.17	0.09	0.27	0.06	0.09	-
MgO	4.86	5.42	4.62	3.25	2.96	4.27	1.94	1.04	1.51	1.5	1.98	2.65	1.91	1.97	1.27	4.31	3.24	0.22
CaO	7.85	8.1	9.69	7.86	6.66	0.97	3.67	2.69	2.97	2.8	3.62	4.12	1.85	4.04	1.13	2.66	0.72	0.07
Na_2O	3.37	2.26	2.34	4.01	3.5	2.66	3.29	3.92	3.39	3.76	3.32	3.46	2.63	3.37	1.84	3.1	1.04	0.18
K_2O	0.54	2.08	1.85	1.67	3.13	3.59	3.29	5.07	4.66	5.6	5.71	5.31	6.36	5.47	10.31	4.65	9.11	0.09
P_2O_5	0.28	0.95	1.02	1.41	0.55	0.2	0.28	0.25	0.29	0.24	0.33	0.39	0.34	0.36	0.34	0.24	0.24	0.02
LOI-Flux	1.94	4.37	2.48	3.72	2.79	2.53	0.73	1.7	2.1	1.43	1.46	2.59	1.48	2.94	1.87	2.91	2.2	1.43
Trace Elements																		
Cr	273	268	271	138	267	342	251	NA	193	178	186	228	372	257	270	690	466	396
Co	58	130	114	56	50	68	NA	41	34	1	2	76	72	NA	76	112	87	12
Ni	53	256	59	NA	34	128	61	16	30	NA	10	21	119	54	64	175	111	60
Cu	237	291	266	298	195	12302	344	NA	134	72	159	109	13613	766	23547	1048	8448	210
Zn	248	324	232	151	97	58	61	143	96	114	166	61	640	112	146	12	16	2
Rb	NA	115	NA	NA	115	135	124	184	197	232	189	255	279	204	330	179	259	-
Sr	461	1841	1252	2108	1078	297	815	644	688	1068	1491	1348	1440	1400	462	644	137	-
Y	33	35	61	55	27	NA	23	54	41	NA	NA	NA	NA	19	4	21	NA	17
Zr	79	247	119	304	353	162	133	360	243	132	325	393	240	469	319	228	194	10
Nb	31	15	62	192	6	13	20	12	20	23	NA	52	62	20	27	34	24	5
Ba	609	2034	1480	2346	1327	2645	1518	2086	1635	542	2042	1430	2833	1520	3027	1925	2792	226
Mo	15	NA	NA	24	NA	NA	NA	NA	NA	13	NA	NA	7	NA	12	33	85	5
W	47	NA	58	55	6	50	65	NA	4	25	NA	NA	NA	NA	80	56	NA	11
Yb	NA	114	NA	7	NA	NA	NA	71	98	31	73	162	67	80	NA	25	113	-
Pb	21	76	67	167	NA	NA	NA	32	82	76	69	114	NA	84	142	62	NA	5
S	509	875	1212	605	718	1600	351	202	620	901	684	233	1052	572	351	872	1545	281
Cl	379	267	271	256	519	727	282	293	487	739	982	710	1012	646	2608	607	742	421
Ratios																		
Na	2.50	1.68	1.74	2.98	2.60	1.97	2.44	2.91	2.52	2.79	2.46	2.57	1.95	2.50	1.37	2.30	0.77	-
K	0.45	1.73	1.54	1.39	2.60	2.98	2.73	4.21	3.87	4.65	4.74	4.41	5.28	4.54	8.56	3.86	7.56	-
K/Na	0.18	1.03	0.88	0.47	1.00	1.51	1.12	1.45	1.54	1.67	1.92	1.72	2.71	1.82	6.27	1.68	9.80	-
K_2O/Na_2O	0.16	0.92	0.79	0.42	0.89	1.35	1.00	1.29	1.37	1.49	1.72	1.53	2.42	1.62	5.60	1.50	8.76	-
Rb/Sr	-	0.06	-	-	0.11	0.45	0.15	0.29	0.29	0.22	0.13	0.19	0.19	0.15	0.71	0.28	1.89	-
mg	31.44	38.87	34.94	25.28	36.37	55.01	31.52	22.25	25.52	43.18	39.85	44.68	31.87	40.90	22.78	43.02	45.21	-
A/NK	2.21	2.38	2.55	1.77	1.72	1.87	1.71	1.25	1.47	1.18	1.25	1.32	1.21	1.27	0.95	1.42	1.19	-
A/CNK	0.66	0.69	0.63	0.65	0.74	1.54	0.98	0.89	0.98	0.83	0.80	0.80	0.93	0.77	0.83	0.96	1.07	-

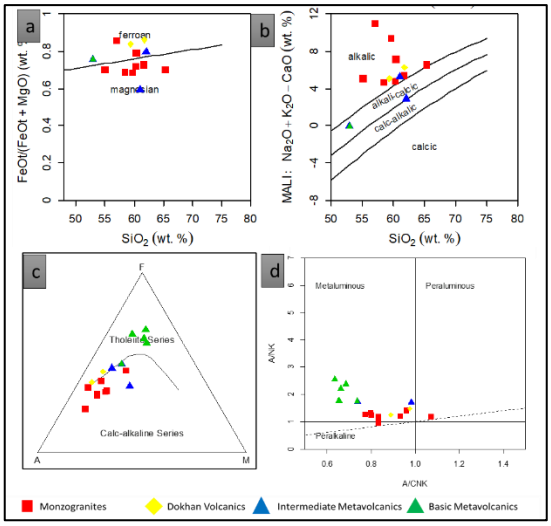

Fig. 16. (a-b). Plots of the studied samples on Frost et al. (2008). c) Irvine and Baragar diagram (1971). d) A/NK versus A/CNK diagram of Shand (1943).

a) Correlation relationships

The plotted geochemical binary relationships of the analyzed elements versus Fe_2O_3 and Cu of all samples distinguished presence of more than one correlation fields pointing to presence of these metals more than one phase e.g. sulfides, oxides and silicates (Figs.18 & 19).

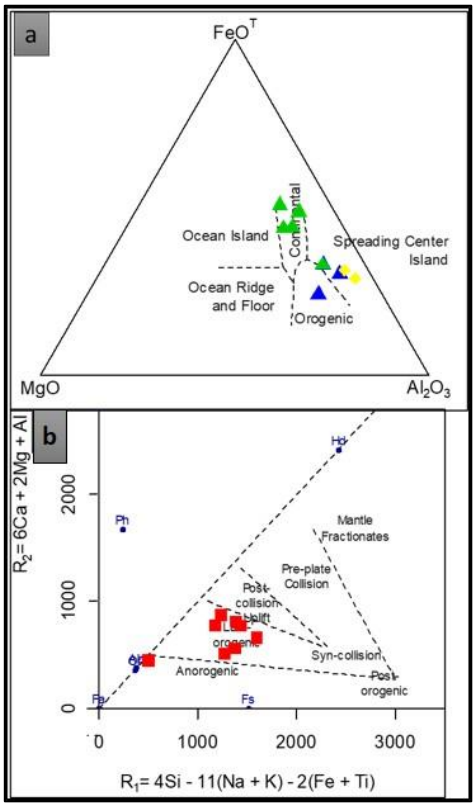

Fig. 17. a) Ternary diagram of Pearce et al. (1977). b) R1-R2 binary diagram of Batchelor & Bowden (1985).

The correlation coefficient (r) matrix of metavolcanics (Table 3) shows significant correlated pairs of elements. The total iron FeO^t shows strong positive correlations with TiO_2, Y, Zn, Mo, and Pb and medium positive correlation with, Nb, Sr, and Co. Other elements such as Rb, Cr, Cu, Ba, and S show strong to medium negative correlation with the total iron FeO^t. The Cu shows strong positive correlation with Cr, Ba, and S while negative correlation with FeO^t, TiO_2, Zn, and Sr. The Ba shows medium positive correlation with Cu and S.

For the monzogranites (Table 4), FeO^t shows very strong positive correlations with Cr, Co, and Ni and medium positive correlation with Y, Ba, and W. Other elements such as Sr show negative correlation with FeO^t. The Cu shows a very strong positive correlation with Rb, Ba, and Cl and medium positive correlation with Co, W, and Zn. The Ba shows strong positive correlation with Cu and FeOt and medium positive correlation with TiO_2, Co Ni, Rb, and Cl.

b) The Clarke of concentration

The calculated Clarke of concentration values for the arc MVs samples are shown in table (5). The reference value is mafic rocks (Turekian & Wedepohl, 1961) and intermediate rocks (Vinogradov, 1962). The intermediate arc MVs are distinguished by Cu CC values up to 351 supporting presences Cu deposits. The Pb CC values range (4 – 28). The Mo CC values reach up to 16 in the basic metavolcanics. Other elements (Co – Ni – Zn) are distinguished near normal CC values.

The calculated Clarke of concentration values for the monzogranite samples are shown in table (6). The reference value is high calcium and low calcium granites (Turekian & Wedepohl, 1961). The monzogranites are distinguished by Cu CC values up to 1361 and 2355 supporting presences of Cu deposits. The Mo CC values reach up to 33 and 65. The Co CC values are very high up to 87 and 76. While the Ni CC values up to 25. The Pb CC values range (4 – 8).

c) Geochemical pathfinders

The arrangement of CC values can be used in the form $\frac{A}{B}$ C (D) where A is the symbol of the chief element, B is the principal associated element having, C is the associated elements, and D is the elements having CC value < 1.

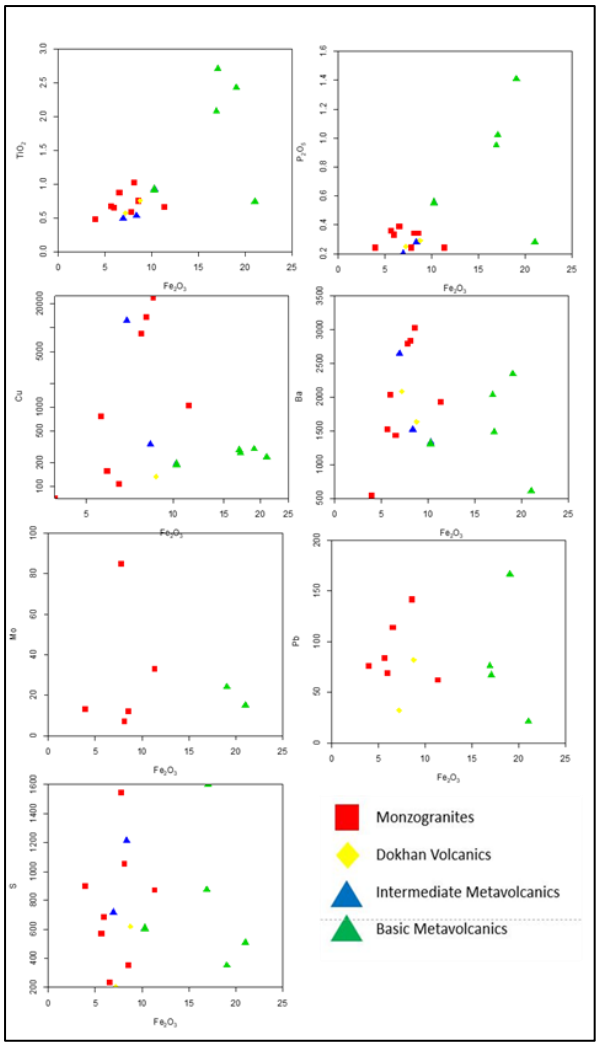

Fig. 18. The binary relationships of the Fe_2O_3 versus trace elements of the analysed samples.

The geochemical spectrum of basic MVs samples recognizes Pb occupying A while Mo is the principal associated element. The Ba and Cu considered as the associated elements. All the other elements (Ni, Zn, Co) are occupying D and exhibit normal dispersed content. The formula of geochemical spectrum can be expressed as:

$$\frac{Pb}{Mo} Ba, Cu\ [Ni, Zn, Co].$$

The geochemical spectrum of intermediate MVs samples recognizes Cu occupying A. The Ba, Mo and Co considered as the associated elements. The other elements (Ni, Zn) occupying D and exhibit normal dispersed content. The formula of geochemical spectrum can be expressed as:

$$\frac{Cu}{\quad} Ba, Mo, Co\ [Ni, Zn].$$

Meanwhile, the geochemical spectrum of monzogranite samples recognizes Cu as the chief ore element and Co as the principal associated element. The recorded elements (Mo, Ni) occupying the C sites are the associated elements of the Cu mineral deposit, while the elements (Ba, Zn, Pb) exhibit near normal dispersed content. The formulae of geochemical spectrum can be expressed as:

$$\frac{Cu}{Co} Mo, Ni[\ Zn, Ba, Pb].$$

Discussion

The current study represents results of the geological-geochemical exploratory works on the SUM area, in which the Cu-Au mineralization is recorded by several published studies. These studies mentioned the geologic mapping for rock units and its petrographic as well as petrochemical characteristics, in addition to age dating of some rock units (Osman, 1994; Botros & Wetait, 1997; Abd El-Rahman et al., 2018).

The field observations, remote sensing data processing, petrographical and ore microscopical studies, chemical analysis of representative rock samples and lithogeochemical exploration survey aimed to define the lithological units and the mineralized outcrops. The defined rock units are arc MVs, DVs, and monzogranite crossed cut by mafic, felsic, the post granitic dykes, and quartz veins. The geochemical behavior of Fe and Cu is investigated, to evaluate the economic importance of these ore elements, using several parameters and factors such as correlation patterns, CC, and pathfinder elements.

The RS processing using ASTER and Sentinel 2B distinguished the presence of co-magmatic alteration types viz propylitic, phyllic, and argillic. The propylitic: (450 to 600ºC) mapped using BR (6+9/8) and Cl index. The phyllic (200 to 450ºC) mapped using BR (7/6) and the OH index. The argillic (100 and 300ºC) mapped using the BR (4/6) and KI index. The used BRs and mineral indices define the sites of the alteration types which co-magmatic. The ferruginous alteration mapped using BR for both the ASTER and Sentinel 2B which indicated the same sites, but Sentinel 2B is preferred due to the higher resolution. Geochemically, the Cu is occupying A while Pb is the principal associated element. Ba and Mo considered as the associated elements. While the geochemical spectrum of monzogranite samples recognizes Cu as the chief ore element and Co as the principal associated.

Table 3. The correlation coefficient (r) matrix of metavolcanics.

	FeOt	*TiO_2*	*Cr*	*Co*	*Ni*	*Cu*	*Zn*	*Rb*	*Sr*	*Y*	*Zr*	*Nb*	*Ba*	*Mo*	*W*	*Yb*	*Pb*	*S*	*Cl*
FeOt	1.00																		
TiO_2	0.61	1.00																	
Cr	-0.50	-0.53	1.00																
Co	0.44	0.66	0.18	1.00															
Ni	-0.08	0.04	0.47	0.61	1.00														
Cu	-0.58	-0.43	0.60	0.00	0.23	1.00													
Zn	0.80	0.59	-0.09	0.77	0.48	-0.47	1.00												
Rb	-0.84	-0.57	0.52	-0.20	0.51	0.44	-0.44	1.00											
Sr	0.47	0.82	-0.76	0.38	0.09	-0.54	0.43	-0.27	1.00										
Y	0.75	0.87	-0.68	0.37	-0.30	-0.72	0.54	-0.79	0.70	1.00									
Zr	-0.10	0.23	-0.43	0.04	-0.05	-0.16	-0.14	0.24	0.60	0.09	1.00								
Nb	0.50	0.61	-0.87	-0.02	-0.49	-0.23	0.04	-0.66	0.64	0.64	0.27	1.00							
Ba	-0.36	0.20	-0.06	0.18	0.31	0.61	-0.28	0.36	0.31	-0.22	0.36	0.31	1.00						
Mo	0.66	0.25	-0.75	-0.17	-0.50	-0.25	0.13	-0.70	0.35	0.42	0.11	0.82	-0.03	1.00					
W	-0.02	-0.05	-0.16	-0.44	-0.55	0.17	-0.38	-0.40	-0.29	0.12	-0.61	0.39	0.02	0.30	1.00				
Yb	0.24	0.34	0.01	0.63	0.87	-0.18	0.67	0.28	0.52	0.06	0.23	-0.17	0.24	-0.20	-0.67	1.00			
Pb	0.65	0.82	-0.81	0.35	-0.11	-0.33	0.40	-0.59	0.86	0.73	0.34	0.90	0.36	0.68	0.08	0.26	1.00		
S	-0.30	0.11	0.60	0.54	0.35	0.77	-0.06	0.19	-0.23	-0.27	-0.10	-0.19	0.55	-0.41	-0.02	0.02	-0.11	1.00	
Cl	-0.62	-0.63	0.67	-0.14	0.05	0.84	-0.55	0.50	-0.67	-0.80	0.05	-0.44	0.27	-0.31	-0.11	-0.32	-0.59	0.60	1.00

Table 4. The correlation coefficient (r) matrix of monzogranites.

	FeOt	*TiO_2*	*Cr*	*Co*	*Ni*	*Cu*	*Zn*	*Rb*	*Sr*	*Y*	*Zr*	*Nb*	*Ba*	*Mo*	*W*	*Yb*	*Pb*	*S*	*Cl*
FeOt	1.00																		
TiO_2	0.31	1.00																	
Cr	0.87	0.02	1.00																
Co	0.87	0.38	0.77	1.00															
Ni	0.89	0.22	0.95	0.77	1.00														
Cu	0.37	0.38	0.05	0.40	0.26	1.00													
Zn	0.00	0.70	-0.13	-0.04	0.12	0.39	1.00												
Rb	0.07	0.42	-0.22	0.32	-0.04	0.87	0.34	1.00											
Sr	-0.49	0.39	-0.54	-0.59	-0.48	-0.44	0.46	-0.33	1.00										
Y	0.43	-0.16	0.53	0.11	0.49	-0.24	-0.31	-0.51	-0.06	1.00									
Zr	-0.11	0.35	-0.33	-0.23	-0.25	-0.09	-0.08	-0.07	0.45	0.33	1.00								
Nb	0.33	0.78	0.25	0.57	0.38	0.25	0.51	0.42	0.11	-0.11	-0.06	1.00							
Ba	0.61	0.45	0.35	0.55	0.53	0.79	0.36	0.54	-0.42	-0.13	0.01	0.17	1.00						
Mo	0.36	-0.38	0.59	0.50	0.52	0.13	-0.35	0.07	-0.83	-0.05	-0.53	-0.08	0.36	1.00					
W	0.51	-0.15	0.30	0.38	0.28	0.51	-0.23	0.31	-0.54	0.31	-0.19	-0.05	0.21	0.02	1.00				
Yb	-0.26	0.27	-0.17	0.04	-0.22	-0.41	-0.11	-0.09	0.27	-0.30	0.36	0.25	-0.12	0.09	-0.78	1.00			
Pb	-0.14	-0.06	-0.43	-0.16	-0.49	0.08	-0.41	0.18	0.08	0.15	0.49	-0.19	-0.27	-0.55	0.52	-0.20	1.00		
S	0.14	-0.29	0.47	0.18	0.47	0.00	0.12	-0.11	-0.43	-0.13	-0.69	-0.04	0.25	0.79	-0.28	0.00	-0.90	1.00	
Cl	0.19	0.19	-0.22	0.15	-0.08	0.86	0.14	0.75	-0.32	-0.21	0.08	-0.06	0.56	-0.15	0.68	-0.52	0.51	-0.37	1.00

Table 5. Clark of concentration of the metavolcanics samples.

Elements	Average		Basic MVs					Intermediate MVs	
	Basic	Intermediate	**45.00**	**55.10**	**71.00**	**72.00**	**70.00**	**64.00**	**67.00**
Co	**48**	**10**	1.21	2.71	2.38	1.17	1.04	6.80	-
Ni	**130**	**55**	0.41	1.97	0.45	-	0.62	2.33	1.11
Cu	**87**	**35**	2.72	3.34	3.06	3.43	2.24	351.49	9.83
Zn	**105**	**72**	2.36	3.09	2.21	1.44	0.92	0.81	0.85
Ba	**330**	**650**	1.85	6.16	4.48	7.11	4.02	4.07	2.34
Mo	**1.5**	0.9	10.00	-	-	16.00	-	-	-
Pb	**6**	**15**	3.50	12.67	11.17	27.83	-	-	-

Table 6. Clark of concentration of the monzogranite samples.

Elements	Average		Monzogranites							
	Low Ca	**High Ca**	**46.1**	**49.1**	**58**	**51**	**52**	**53**	**54**	**65**
Co	1	7	0.1	0.3	10.9	72.0	-	76.0	16.0	87.0
Ni	4.5	15	-	0.7	1.4	26.4	3.6	14.2	11.7	24.7
Cu	10	30	2.4	5.3	3.6	1361.3	25.5	2354.7	34.9	844.8
Zn	39	60	1.9	2.8	1.0	16.4	1.9	3.7	0.2	0.4
Ba	840	420	1.3	4.9	3.4	3.4	3.6	3.6	4.6	3.3
Mo	1.3	1	13.0	-	-	5.4	-	9.2	33.0	65.4
Pb	19	15	5.1	4.6	7.6	-	5.6	7.5	4.1	-

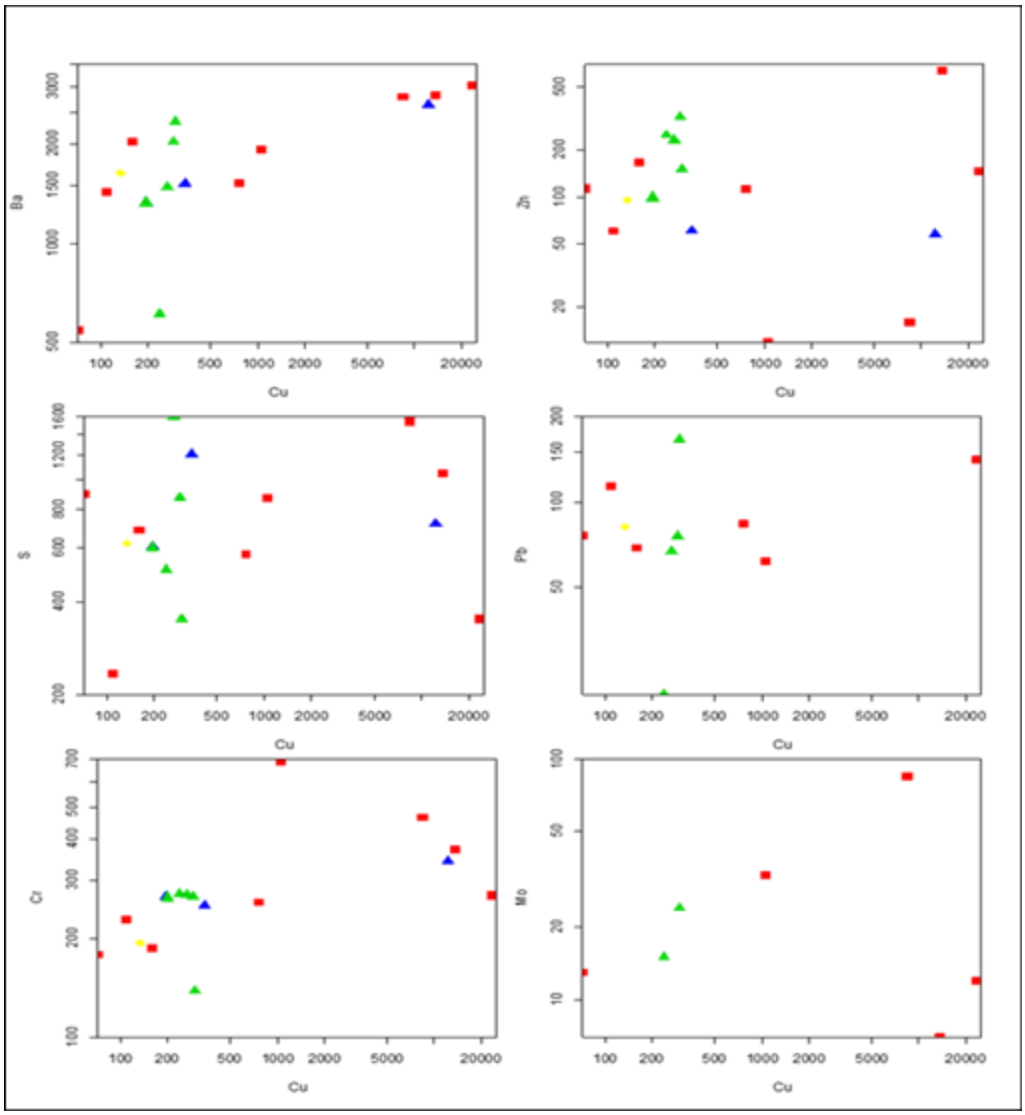

Fig. 19. The binary relationships of the Cu Vs trace elements of the analyzed samples.

The wide distribution of both primary and secondary iron minerals in the area pointing to the genesis of mineralization related to iron oxides apatite (IOA) (also known as Kiruna type) and iron oxides copper gold (IOCG). According to Hitzman et al. (1992) the two types of mineral deposits are very similar in tectonic settings, mineralization and alteration, igneous host rocks, and considered IOA deposits as a subclass of IOCG deposits.

The features of IOA and IOCG according to Hitzman (2000) are: no specific time for formation of the deposits, three distinctive tectonic setting, which are a) intracontinental orogenic; (b) intracontinental anorogenic magmatism; and (c) extension along a subduction-related continental margin, association with igneous activity such as intrusions and dykes, abundance of iron oxide minerals and a relative lack of iron sulfides, both types may contain significant carbonate, Ba, P, or F. The iron oxide-Cu-Au deposits may contain a suite of minor metals including U, Ag, Mo, Co, As, and Zn and anomalous concentrations of REEs, the alteration types in IOA deposits are generally spatially associated with zones of sodic or sodic-calcic alteration, while IOCG associated with sodic-potassic, potassic, or hydrolytic alteration depending on the degree of interaction with meteoric or connate fluids.

The recorded ore minerals in the arc MVs are mainly magnetite with Ti-magnetite in addition to apatite (Figs.11a). Meanwhile in IOCG, the ore minerals are chalcopyrite, pyrite, magnetite, and hematite (Figs.13 & 14). The host rocks were formed within the late orogenic granites or continental and orogenic for metavolcanics. Also, the wide distribution of barite in the area and high content of P in the samples and recorded thorite as well as Cd- Se mineral which are features related to IOCG.

Moreover, the area is abundant in different types of dykes such as basic, felsic, and granitic composition. The alteration types are sodic alteration that was recorded by Botros & Wetait, (1997) and Abd El-Rahman et al. (2018) but not abundant, while the potassic alteration and hydrolytic alteration were recorded.

From the previous results, the suggested genesis of the mineralization are two phases: the first is IOA that are rich in Ti-magnetite and apatite mainly in metavolcanics followed by IOCG, which is rich in magnetite, hematite and Cu sulfides. Au also recorded in previous works (Botros & Wetait, 1997; Abd El-Rahman et al., 2018; Abdelnasser et al., 2023).

Conclusions

The recorded conclusions are as follows:

1- The rock units at SUM area are represented by metavolcanics, dokhan volcanics, and monzogranites. The MVs are meta-basalt and meta-andesite. The DVs are represented mainly by andesite and dacite. Monzogranites are medium to coarse grained consist of plagioclase, quartz, orthoclase and biotite as essential minerals. Sphene, zircon and apatite are the accessory minerals.

2 - The lineaments and rose diagram indicated two main structural trends at NW-SE and NE-SW directions, while for the lithological mapping, the ASTER and Sentinel-2B data were processed using the optimum index factor (OIF), false colour composite (FCC) and band ratios techniques. Based on the OIF results, the ASTER band combinations (R: 8, G: 6, B: 1) and (R: 9, G: 2, B: 1), along with the Sentinel-2B band combinations (R: 12, G: 11, B: 2) and (R: 12, G: 4, B: 2), effectively distinguish the various rock units present in the area.

3- The mineral indices (Kl, OH, Cl) and band ratios (4/6, 7/6, 6+9/8) identified the hydrothermal alterationzones such as argillic, phyllic, and propylitic which are pointing to hydrothermal co-magmatic origin.

4 - Geochemically, the rocks are ferroan to magnesian and alkaline for most rocks except intermediate DVs. The monzogranites, intermediate MVs, and DVs samples showing calc-alkaline while basic MVs showing tholeiitic field. The samples are metaluminous except for one sample which is peraluminous. For the monzogranites, total iron shows very strong positive correlations with Cr, Co, and Ni. The Cu shows a very strong positive correlation with Rb, Ba, and Cl. The binary relationship distinguished between two fields of ore elements pointing to the presence of these metals more than one phase e.g. sulfides, oxides and silicates. The geochemical spectrum recognizes Cu as the chief ore element for both metavolcanics and monzogranites.

5- The detected ore minerals are mainly iron and copper minerals including chalcopyrite, pyrite, magnetite, hematite (Specularite), titanomagnetite, and ilmenite. The secondary minerals are covellite, malachite, chrysocolla, atacamite and goethite. Other recorded minerals are barite, chromite, monazite, thorite, molybdenite, and Cd-Se minerals.

Acknowledgements:

The authors gratefully acknowledge the Nuclear Materials Authority (NMA) for facilitating fieldwork

activities and logistical support. We further extend our gratitude to Dr. Abd El Hady Radwan lecturer of basement rocks and Dr. Mohamed Hassan lecturer of structural geology at Aswan University for their essential contributions during field works. Additionally, we sincerely appreciate the chemical analytical assistance provided by Dr. Tamer Hamed El Saied at the Exploration Department, Egyptian Petroleum Research Institute, Cairo, Egypt.

References

Abd El-Rahman, Y., Seifert, T., Gutzmer, J., Said, A., Hofmann, M., Gärtner, A., & Linnemann, U. (2017). The South Um Mongul Cu-Mo-Au prospect in the Eastern Desert of Egypt: From a mid-Cryogenian continental arc to Ediacaran post-collisional appinite-high Ba-Sr monzogranite. *Ore Geology Reviews*, *80*, 250–266. https://doi.org/10.1016/j.oregeorev.2016.06.004

Abd El-Rahman, Y., Seifert, T., & Said, A. (2018). The South Um Mongul Cu-Mo-Au prospect in the northern Eastern Desert of Egypt: Tonian porphyry-style mineralization with an Ediacaran hydrothermal iron oxide overprint. *Ore Geology Reviews*, *99*, 217–234. https://doi.org/10.1016/j.oregeorev.2018.06.011

Abdelnasser, A., Khedr, L., Kharbish, S., Zoheir, B., & Zamzam, S. (2023). Sulfide disseminations and hydrothermal alteration haloes in the Gabal Monqul area, Egypt: Field, mineralogical, and remote sensing studies. *Journal of African Earth Sciences*, *199*, 104830. https://doi.org/10.1016/J.JAFREARSCI.2023.104830

Abrams, M. J., & Brown, D. (1984). Silver Bell, Arizona, porphyry copper test site report: Tulsa, Oklahoma. *The American Association of Petroleum Geologists, the Joint NASA–Geosat Test Case Project, Final Report*, 4–73.

Abrams, M. J., Brown, D., Lepley, L., & Sadowski, R. (1983). Remote sensing for porphyry copper deposits in southern Arizona. *Economic Geology*, *78*(4), 591–604. https://doi.org/10.2113/GSECONGEO.78.4.591

Adiri, Z., Lhissou, R., El Harti, A., Jellouli, A., & Chakouri, M. (2020). Recent advances in the use of public domain satellite imagery for mineral exploration: A review of Landsat-8 and Sentinel-2 applications. *Ore Geology Reviews*, *117*, 103332. https://doi.org/10.1016/J.OREGEOREV.2020.103332

Batchelor, R. A., & Bowden, P. (1985). Petrogenetic interpretation of granitoid rock series using multicationic parameters. *Chemical Geology*, *48*(1–4), 43–55. https://doi.org/10.1016/0009-2541(85)90034-8

Bentor, Y. K. (1985). The crustal evolution of the Arabo-Nubian Massif with special reference to the Sinai Peninsula. *Precambrian Research*, *28*(1), 1–74. https://doi.org/10.1016/0301-9268(85)90074-9

Botros, N. S., & Wetait, M. A. (1997). Possible porphyry copper mineralization in south Um Monqul, Eastern Desert, Egypt. *Egypt J Geol*, *41*(1), 175–196.

Breitkreuz, C., Eliwa, H., Khalaf, I., Gameel, K. El, Bühler, B., Sergeev, S., Larionov, A., & Murata, M. (2010). Neoproterozoic SHRIMP U-Pb zircon ages of silica-rich Dokhan Volcanics in the North Eastern Desert, Egypt. *Precambrian Research*, *182*(3), 163–174. https://doi.org/10.1016/j.precamres.2010.06.019

Chavez, P., Berlin, G., & Sowers, L. (1982). *STATISTICAL METHOD FOR SELECTING LANDSAT MSS RATIOS*.

del Real, I., Reich, M., Simon, A. C., Deditius, A., Barra, F., Rodríguez-Mustafa, M. A., Thompson, J. F. H., & Roberts, M. P. (2023). Formation of giant iron oxide-copper-gold deposits by superimposed episodic hydrothermal pulses. *Scientific Reports 2023 13:1*, *13*(1), 1–13. https://doi.org/10.1038/s41598-023-37713-w

El-Desoky, H.M., Hafez M.H. (2018). Petrology, Geochemistry and Mineralogy of the Hydrothermally Altered Rock Units at Wadi Dara, North Eastern Desert, Egypt. Annals Geol. Surv. Egypt. V. XXXV (2018), pp. 103 – 140.

Eliwa, H. A., Breitkreuz, C., Murata, M., Khalaf, I. M., Bühler, B., Itaya, T., Takahashi, T., Hirahara, Y., Miyazaki, T., Kimura, J. I., Shibata, T., Koshi, Y., Kato, Y., Ozawa, H., Daas, M. A., & El Gameel, K. (2014). SIMS zircon U–Pb and mica K–Ar geochronology, and Sr–Nd isotope geochemistry of Neoproterozoic granitoids and their bearing on the evolution of the north Eastern Desert, Egypt. *Gondwana Research*, *25*(4), 1570–1598. https://doi.org/10.1016/J.GR.2013.06.006

Emam, A., Hamimi, Z., El-Fakharani, A., Abdel-Rahman, E., Barreiro, J. G., & Abo-Soliman, M. Y. (2018). Utilization of ASTER and OLI data for lithological mapping of Nugrus-Hafafit area, South Eastern Desert of Egypt. *Arabian Journal of Geosciences*, *11*(23), 1–22. https://doi.org/10.1007/S12517-018-4106-1/FIGURES/14

Forson, E. D., Menyeh, A., & Wemegah, D. D. (2021). Mapping lithological units, structural lineaments and alteration zones in the Southern Kibi-Winneba belt of Ghana using integrated geophysical and remote sensing datasets. *Ore Geology Reviews*, *137*, 104271. https://doi.org/10.1016/J.OREGEOREV.2021.104271

Frost, B. R., & Frost, C. D. (2008). A Geochemical Classification for Feldspathic Igneous Rocks. *Journal of Petrology*, *49*(11), 1955–1969. https://doi.org/10.1093/PETROLOGY/EGN054

Gass, I., & Ed, T. R. (1982). Upper Proterozoic (Pan-African) Calc-Alkaline Magmatism in North-Eastern Africa and Arabia.

Hassaan, M. M., Azzaz, S. A., Soliman, M. M., & El-Badawy. (1991). Use of Some Statistical and Geochemical Parameters in Solving Some Genetic Problems of Sukkari Gold Mineralization, Egypt. *48th I-S.I. Sess.,Cairo*, 9–17.

Hassaan, M. M., Omar, S. A., Khalil, A. E., Shahin, T. M., El-Naggar, I. M., Sayyed, M. I., & Hanfi, M. Y. (2022). Prognostic Exploration of U-F-Au-Mo-W Younger Granites for Geochemical Pathfinders, Genetic Affiliations, and Tectonic Setting in El-Erediya-El-Missikat Province, Eastern Desert, Egypt. *Minerals*

2022, Vol. 12, Page 518, *12*(5), 518. https://doi.org/10.3390/MIN12050518

Hassaan, M. M., Soliman, M. M., Azzaz, S. A., & Attawiya, M. Y. (1990). Geological Studies on Gold Mineralization at Sukkari, Um Ud and Samut, Eastern Desert, Egypt. *Annals of the Geological Survey of Egypt*, *16*, 89–95. https://www.scirp.org/reference/referencespapers?referenceid=2002615

Hassaan, Mahmoud. (2011). *METALLIC ORE DEPOSITS OF THE NUBIAN SHIELD IN EGYPT*. LAP LAMBERT ACADEMIC PUBL.

Hitzman, M. W. (2000). *IRON OXIDE-Cu-Au DEPOSITS: WHAT, WHERE, WHEN AND WHY*.

Hitzman, M. W., Oreskes, N., & Einaudi, M. T. (1992). Geological characteristics and tectonic setting of proterozoic iron oxide (Cu□U□Au□REE) deposits. *Precambrian Research*, *58*(1–4), 241–287. https://doi.org/10.1016/0301-9268(92)90121-4

Irvine, T. N., & Baragar, W. R. A. (1971). A Guide to the Chemical Classification of the Common Volcanic Rocks. *Canadian Journal of Earth Sciences*, *8*(5), 523–548. https://doi.org/10.1139/E71-055

Jensen, L. S. (1976). New Cation Plot for Classifying Subalkalic Volcanic Rocks. *Ontario Division Mines, Miscellaneous Paper*, *66*, 1–22.

Kviatkovisky, E. M. (1977). *Lithochemical methods of prospecting for endogeneous ore deposits*. Leningrad Nedra.

Sultan, M., Arvidson, R.E & Sturchio, N.C (1986). *Mapping of serpentinites in the Eastern Desert of Egypt by using Landsat thematic mapper data | Geology | GeoScienceWorld*. Geology,14. https://pubs.geoscienceworld.org/gsa/geology/article-abstract/14/12/995/204033/Mapping-of-serpentinites-in-the-Eastern-Desert-of

Middlemost, E. A. K. (1994). Naming materials in the magma/igneous rock system. *Earth-Science Reviews*, *37*(3–4), 215–224. https://doi.org/10.1016/0012-8252(94)90029-9

Ninomiya, Y. (2003). A Stabilized Vegetation Index and Several Mineralogic Indices Defined for ASTER VNIR and SWIR Data. *International Geoscience and Remote Sensing Symposium (IGARSS)*, *3*, 1552–1554. https://doi.org/10.1109/igarss.2003.1294172

Osman, A. (1994). Native Gold Mineralization Associated with Iron Oxides, Mongul Area, Northern Eastern Desert, Egypt. *Earth Science Series*, 74–87.

Pearce, T. H., Gorman, B. E., & Birkett, T. C. (1977). The relationship between major element chemistry and tectonic environment of basic and intermediate volcanic rocks. *Earth and Planetary Science Letters*, *36*(1), 121–132. https://doi.org/10.1016/0012-821X(77)90193-5

Pieri, D., & Abrams, M. (2004). ASTER watches the world's volcanoes: A new paradigm for volcanological observations from orbit. *Journal of Volcanology and Geothermal Research*, *135*(1), 13–28. https://doi.org/10.1016/j.jvolgeores.2003.12.018

Pirajno, F. (2009). Hydrothermal Processes and Wall Rock Alteration. *Hydrothermal Processes and Mineral Systems*, 73–164. https://doi.org/10.1007/978-1-4020-8613-7_2

Pohl, W. L. (2011). Economic Geology Principles and Practice: Metals, Minerals, Coal and Hydrocarbons - Introduction to Formation and Sustainable Exploitation of Mineral Deposits. In *Economic Geology Principles and Practice: Metals, Minerals, Coal and Hydrocarbons - Introduction to Formation and Sustainable Exploitation of Mineral Deposits*. Wiley-Blackwell. https://doi.org/10.1002/9781444394870

Ridley, J. (2013). Hydrothermal ore deposits I: magmatic and orogenic environments. In *Ore Deposit Geology* (pp. 92–240). Cambridge University Press. https://doi.org/10.1017/cbo9781139135528.004

Seedorff, E., Dilles, J. H., Proffett, J. M., Einaudi, M. T., Zurcher, L., Stavast, W. J. A., Johnson, D. A., & Barton, M. D. (2005). Porphyry Deposits: Characteristics and Origin of Hypogene Features. *One Hundredth Anniversary Volume*. https://doi.org/10.5382/AV100.10

Shand, S. J. (1943). *Eruptive Rocks. Their Genesis, Composition, Classification, and Their Relation to Ore-Deposits with a Chapter on Meteorite*. John Wiley & Sons, New York.

Shebl, A., & Csámer, Á. (2021). Reappraisal of DEMs, Radar and optical datasets in lineaments extraction with emphasis on the spatial context. *Remote Sensing Applications: Society and Environment*, *24*. https://doi.org/10.1016/J.RSASE.2021.100617

Skirrow, R. G. (2022). Iron oxide copper-gold (IOCG) deposits – A review (part 1): Settings, mineralogy, ore geochemistry and classification. *Ore Geology Reviews*, *140*, 104569. https://doi.org/10.1016/J.OREGEOREV.2021.104569

Spatz, D. M., Wilson, R. T., Pierce, F. W., & Bolm, J. G. (1995). Remote sensing characteristics of porphyry copper systems, western America Cordillera. *Arizona Geological Society Digest*, *20*, 94–108.

Stern, R. J., & Hedge, C. E. (1985). Geochronologic and isotopic constraints on late Precambrian crustal evolution in the Eastern Desert of Egypt. *American Journal of Science*, *285*(2), 91–127. https://doi.org/10.2475/AJS.285.2.97

Stern, R. J., & Kröner, A. (1993). Late Precambrian Crustal Evolution in NE Sudan: Isotopic and Geochronologic Constraints. In *Source: The Journal of Geology* (Vol. 101, Issue 5). http://www.jstor.orgURL:http://www.jstor.org/stable/

Turekian, K. K., & Wedepohl, K. H. (1961). Distribution of the Elements in Some Major Units of the Earth's Crust. *GSA Bulletin*, *72*(2), 175–192. https://doi.org/10.1130/0016-7606(1961)72[175:DOTEIS]2.0.CO;2

van der Werff, H., & van der Meer, F. (2016). Sentinel-2A MSI and Landsat 8 OLI provide data continuity for geological remote sensing. *Remote Sensing*, *8*(11). https://doi.org/10.3390/rs8110883

Vinogradov A.P (1962). Average contents of chemical elements in the principal types of igneous rocks of the Earth's crust .Geochemistry, pp. 641-664

Wetait, M. A., & Botros, N. S. (1997). Barite mineralisation in the south Um Monqul area, north Eastern Desert, Egypt. *Journal of African Earth Sciences*, *25*(3), 485–489. https://doi.org/10.1016/S0899-5362(97)00118-8

الاستكشاف الجيوكيميائي لتمعدن النحاس بمنطقة جنوب جبل أم منقل، شمال الصحراء الشرقية، مصر

عطيه ربيع [١]، ✉محمد عبدالوهاب جابر [٣]، وطاهر شاهين [١]، وأشرف إمام [٢]، ومحمود محمد حسان [١]

[١] *قسم الجيولوجيا ، كلية العلوم ، جامعة الأزهر ، القاهرة ، مصر*

[٢] *قسم الجيولوجيا ، كلية العلوم ، جامعة أسوان ، أسوان ، مصر*

[٣] *قسم الاستكشاف ، معهد بحوث البترول ، القاهرة ، مصر*

تقع منطقة جنوب جبل أم منقل في الجزء الشمالي من الصحراء الشرقية لمصر، وهي معروفة بتعدين النحاس والذهب.وتتكون الوحدات الصخرية من الصخور البركانية المتحولة، وصخور الدخان البركانية، والمونزوجرانيت. تم إجراء دراسات ميدانية متكاملة، واستشعار عن بعد، ودراسات مجهرية وجيوكيميائية لتحديد التراكيب والوحدات الصخرية ومناطق التحول الحرمائي ودراسة نشأة التمعدن. تمثل الصخور البركانية المتحولة الميتابازلت والميتاأنديسايت ، والتي تظهر نسيجًا دقيقًا وبورفيريًا. تمثل صخور الدخان البركانية الأنديسايت والداسيت. ويتكون المونزوجرانيت بشكل رئيسي من الكوارتز والبلاجيوكليز والأورثوكلاز والبيوتيت.وقد حددت بيانات الاستشعار عن بعد الاتجاهات الرئيسية للتراكيب وهي الشمال الشرقي والشمال الغربي. و لرسم الخرائط الصخرية ونطاقات التحول الحرمائي، استخدمت التقنيات الأتية وهيOIF ، FCC، Band Ratiosوالتي وضحت الوحدات الصخرية و أنواع التحول الحرمائي مثل الأنواع الأرجيلية والفيلية والبروبيلية. جيوكيميائيًا، أظهرت عينات المونزوجرانيت والصخور البركانية المتحولة المتوسطة وصخور الدخان البركانية أنها تنتمي إلى المجال القلوي الكلسي، بينما أظهرت الصخور البركانية المتحولة الأساسية أنها تنتمي إلى المجال الثوليتي. وأظهرت الأنماط والعوامل الجيوكيميائية وجود مجالين ارتباط للعناصر ، مما يشير إلى وجود هذه المعادن في أكثر من طور، مثل الكبريتيدات والأكاسيد والسيليكات. يعتبر النحاس هو العنصر الخام الرئيسي في الصخور البركانية المتحولة؛ والرصاص والموليبدينوم هما العنصران المصاحبان الرئيسيان، بينما الباريوم هو العنصر المصاحب. أما في المونزوجرانيت، يمثل النحاس أيضًا العنصر الخام الرئيسي. المعادن الخام الأولية هي الكالكوبيريت، البيريت، المغنتيت، الهيماتيت، التيتانوماجنتيت، والإلمينيت. المعادن الأخرى المسجلة هي الباريت، الكروميت، المونازيت، الثوريت، الموليبدينيت، ومعادن الكادميوم والسيلينيوم. من ناحية أخرى، المالاكيت، الكريسوكولا، الأتاكاميت، والجيوثيت هي المعادن الثانوية.